Miskolci Egyetem habilitációs füzetei

Tudományos munkásság áttekintő összefoglalása

Mérnöki szerkezetek kísérleteken alapuló végeselemes modellezése és optimalizációja

Írta
Dr. Mankovits Tamás,

aki a Gépészeti Tudományok tudományágban „dr. habil.” cím elnyerésére pályázik

Miskolc
2024

Habilitation booklets of the University of Miskolc

Overview summary of scientific work

Finite element modelling and optimization of engineering structures based on experiments

written by
Dr. Tamás Mankovits,

who is applying for the title "dr. habil." in the discipline of Mechanical Engineering Sciences

Miskolc
2024

Contents

1. Introduction

Finite element modelling and optimization of different engineering structures are indispensable in the engineering design process nowadays since time and cost can be saved. The available professional finite element systems can handle practically all physical phenomena. The accuracy of the finite element computations depends on the finite element model describing the problem. The elaboration of these finite element models is an important engineering task. Depending on the complexity of the problem (e.g. large deformation, nonlinearity, high computational demand, etc.), this task can cause serious challenges to simulation engineers.

In 2013, after the successful defence of my PhD thesis entitled 'Shape optimization of rubber parts', my research activities have been continued in three directions. One direction is the investigation of closed-cell aluminium foams, the second is the investigation of titanium lattice structures, and the third is the continuation of the doctoral topic dealing with rubber parts. Although the three topics are apparently sharply different from each other, they have many things in common, these are:

- typical loading is compression;
- complex problems with sophisticated finite element models (high computational demand, so simplified models are needed for the aluminium foam and titanium structures; handling large deformation and material nonlinearity for rubbers);
- the optimization task arises to ensure the required mechanical properties.

My research was supported by several projects, and due to the nature of the tasks, it was feasible and efficient to work in teams.

On the topic of shape optimization of rubber parts, my PhD student obtained his PhD degree in informatics entitled 'Development of finite element simulation-based optimization of rubber bumper'. Furthermore, another student of mine is completing his PhD studies on the topic of 'Design of patient-specific hip implant using titanium lattice structure' at the Doctoral School of Informatics of the University of Debrecen.

2. Geometrical modelling and finite element analysis of closed-cell aluminium foams

2.1. Brief overview of the research

Aluminium foams have good density specific mechanical properties due to their lightweight cellular structure. It is well known that metal foams have high specific compression strength combined with excellent energy absorption characteristics [1]. Therefore, the interest in these materials is widespread not only as a vibration damper or sound absorber but also as a load-bearing structural element. Numerous applications rely on the compressive properties of metal foams, which directly depend on their structure. As a load-bearing structural element, e.g. vehicle part, metal foam is expected to behave elastically under operational circumstances, so the material response must be predicted precisely in the elastic region. Numerical determination of compressive properties of foam structure remains a demanding engineering task, and it is indispensable for design purposes [2].

The current limitations of its widespread application are the high production cost and the difficult reproducibility due to the production challenges. Moreover, the design difficulties and the still unsolved efficient and reliable finite element technique are also obstacles to the application. Over the recent years, the focus of my research was to find appropriate solutions for the above-mentioned problems.

Based on the needs metal foams can be produced from different raw materials (aluminium, magnesium, titanium, etc.) and can be grouped according to the structure (open-cell, closed-cell, metal matrix syntactic, etc.).

A number of studies have reported on measuring the material response of different types of metal foams in destructive ways. The compressive properties of open-cell metal foams in [3,4], metal matrix syntactic foams in [5,6], and titanium foam in [7] were investigated, while the elastic behaviour of closed-cell aluminium foam under uniaxial loading and bending conditions was also studied in [8].

The geometrical modelling is an essential part of the procedure aiming at the investigation of metal foam structures in a numerical way. Numerous approaches can be found in the literature for the proper geometrical description of foam structures.

One of which is the usage of uniform cell models which results in simplified geometry compared with the actual structure. A combination of spherical and cruciform-shaped cells was used to model closed-cell aluminium foam and to simulate its material response in [9], while different uniform cell structures were applied to the model and simulate open cell metal foams in [10]. Diamond and cubic cell foam structures were also used to simulate the effect of cell shape on the mechanical behaviour of open cell metal foams in [11]. A numerical study using the Weaire-Phelan unit cell was introduced in [12].

Recent studies proved that micro computed tomography (μCT) can be an efficient and powerful tool for mapping the complete structure of materials in a non-invasive and non-destructive way. Three-dimensional models were generated based on μCT images and numerical calculations were performed on cellular structures in [13]. Closed-cell aluminium foams in [14] and open-cell aluminium foams in [15] were investigated numerically based on μCT images and the material response for compression was determined.

The number of publications in the field of geometrical modelling and finite element analysis of metal foam structures demonstrates that this topic is in the focus of studies. To obtain high-quality predictions of a porous material response, it is critical to construct finite element models that provide an adequate description of the actual geometry [2].

During my research two types of closed-cell aluminium foam structures were investigated. One is produced with direct foaming technique called ALUFOAM by the Department of Mechanical Engineering, Faculty of Engineering, University of Debrecen. The other type is called ALUHAB is made by bubble injection process and procured from the Aluinvent Zrt. For modelling these structures the μCT based (for ALUFOAM) and unit cell based (for ALUHAB) techniques are also introduced.

In the case of ALUFOAM, a geometrical reconstruction and finite element analysis of the structure in the elastic region are presented based on μCT images. The degree of deviation between the simulation and measurement results is acceptable according to the engineering practice, proving that the method is suitable for the description of the real structures. An essential part of the procedure is a manual reconstruction method for objects of complex geometry. The first step is the preparation of plane sections (CT images) with parallel planes of a given density. The second is the performance of a series of transformations providing a geometrically accurate three-dimensional object that is suitable for finite element analysis. The investigation of specimens proves that the accuracy of the proposed reconstruction method meets the requirements, and the procedure can be reproduced and validated [2].

In the case of ALUHAB the Weaire-Phelan unit cell was used to model the actual foam specimen. The accuracy of

the created CAD model was validated by comparing its physical properties to the original specimen. The validated model was then used for the finite element simulations focusing on the elastic behaviour. By comparing the finite element simulation results to the laboratory measurement, the accuracy and usability of the simplified model were presented [16].

2.2. Introduction of the investigated structures

The ALUFOAM was produced from Duralcan F3S.20S Metal Matrix Composite and fabricated using a direct foaming technique by adding TiH powder as a blowing agent [2]. The method of the production is described in our works [17,18].
The chemical composition determined by EDX analysis and the related physical and mechanical properties of the applied matrix material can be seen in Table 1.

Table 1. Chemical composition and related physical and mechanical properties of the matrix material [2]

Element	Measured data
Al (wt%)	69.26
Si (wt%)	9.21
Mg (wt%)	0.53
SiC (wt%)	20.8
other (wt%)	0.2
Properties	
SiC median particle size (mm)	13.24
Density (kg/m^3)	2875.12
Young's modulus (GPa)	97.2

The size of the specimens was determined according to the ISO 13314 standard [19] based on a statistical analysis of

the pore sizes. The size of the specimens was 14.5 mm × 14.5 mm × 14.5 mm (see Figure 1) and STRUERS Labotom-15 was used for cutting [2]. The main properties of the specimens are listed in Table 2.

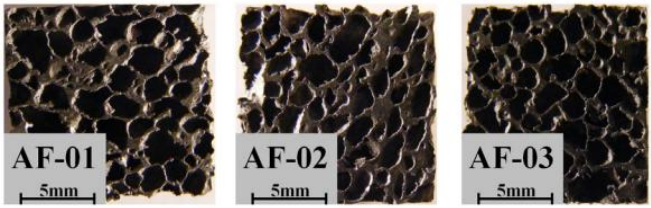

Figure 1. Aluminium foam specimens produced by direct foaming (ALUFOAM) [2]

Table 2. Structural properties (average) of the ALUFOAM specimens

Properties	Measured data	Standard deviation
Mass (g)	1.34	0.015
Porosity (%)	85.31	0.133

The ALUHAB was procured from the Aluinvent Zrt. The chemical composition of the raw material is unfortunately confidential. For the compression test five cylindrical specimens were cut according to the ISO 13314 standard [19]. The diameter and the length were 30 mm, respectively. Table 3 shows the average physical properties of the material. The porosity was calculated based on the weight of the specimens. An image of the specimen is shown in Figure 2. The average cell size and wall thickness were determined using CT analysis [16].

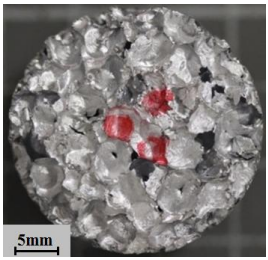

Figure 2. ALUHAB specimen [16]

Table 3. Structural properties (average) of the ALUHAB specimens [16]

Properties	Measured data	Standard deviation
Mass (g)	6.6	0.166
Porosity (%)	89.27	0.26

2.3. Compression tests

Both types of specimens were subjected to a series of compression tests. The compression tests for the aluminium foams produced by direct foaming were performed on an INSTRON 8874 type universal testing machine at room temperature. The compression tests were carried out with the application of lubricant. The deformation rate was maintained in quasi-static condition at 8.7 mm/min. During the tests, the engineering stress-engineering strain curves were registered and processed according to the ruling standard for the compression test for porous and cellular materials [19]. The compressive stress-strain curve of the investigated specimens can be seen in Figure 3 [2].

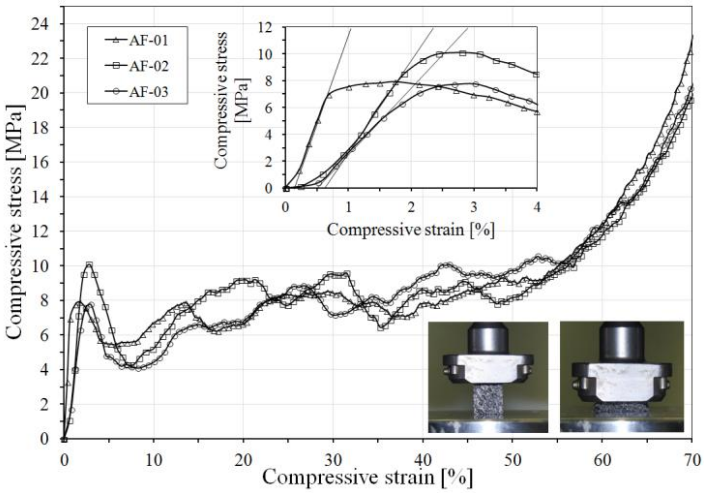

Figure 3. Compressive stress-strain curves of the ALUFOAM specimens [2]

The compression test in the case of ALUHAB was done using the INSTRON 68TM-10 universal material testing system and the strains were measured using the INSTRON AVE2 advanced video extensometer. The specimens were compressed until 0.2% strain which in the case of the whole specimen is 0.06 mm. The load was applied with a 1 mm/min velocity. The results of the 5 compression tests were then summarised and the median value was selected for the comparison with the results of the finite element analysis. The maximum load on this specimen was 162.6 N, the results of the 4 other specimens showed a 3.56% maximum deviation from the median value [16].

2.4. Geometrical modelling of the foam structures

In the case of ALUFOAM, a geometrical reconstruction process was established. The basis of the geometrical

reconstruction was the μCT analysis that was performed using a YXILON CT Modular type industrial CT equipment with an X-ray tube of 225 kV and resolution of 7 μm. Using Materialise Mimics v10.1 and its complement Materialise Magics v9.9, the reconstruction of the samples' geometry was established through some manual steps. The automatic reconstruction was then compared to the manual reconstruction process, and the results of the proposed process were qualified. An evaluation copy of VGStudio Max 3.0 was used to control the quality of the geometric reconstruction. The original structure was then compared to the reconstructed one [2].

Materialise Mimics v10.1 is used for the reconstruction process. This software allows automatic reconstruction, which results in a model that is suitable for finite element analysis, but the accuracy of the geometrical conformity is not high enough. Instead of an automatic reconstruction process, the software allows custom parameter settings defined by the user in each step of the transformation. The order of transformations can be chosen resulting in different model properties. The transformations provide STL files with different properties, e.g. mass, volume and number of elements. Figure 4. shows the order of transformations that was proved to be the best for approximation in the modelling of closed-cell aluminium foams (the figure contains the original command names used in Mimics) [2].

The accuracy of geometry was checked by comparing the foam model provided by the reconstruction process with the model described by the STL file using the evaluation copy of VGStudio Max 3.0. The comparison resulted in a statistical evaluation of deviations [2].

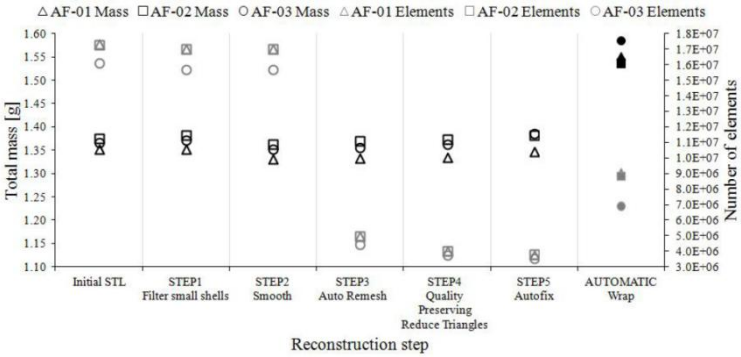

Figure 4. Comparison of the automatic and the parameterized processes (total volume, number of elements) [2]

The benefit of the proposed procedure is the high precision preparation of the foam structure attained by the custom parameterized reconstruction method [2]. Figure 5. shows the complete modelling procedure including the results of the finite element simulations.

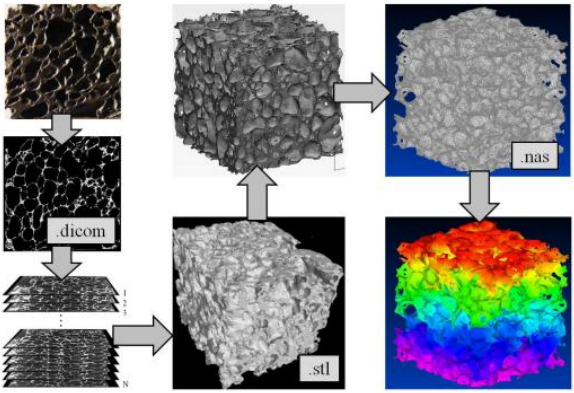

Figure 5. The modelling procedure [2]

For the cell structure approximation of the ALUHAB structure, the Weaire-Phelan unit cell was chosen. The 3D model was created using the SIEMENS Solid Edge software. After several steps, the unit cell was modelled. The unit cells were then multiplied to create a cube with a 30 mm edge length which was then cut to the cylinder shape of the specimen with a 30 mm diameter. The final CAD model of the aluminium foam specimen can be seen in Figure 6 [16].

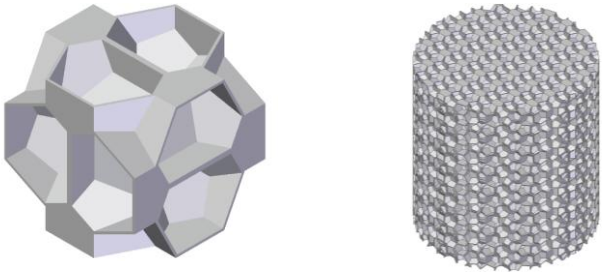

Figure 6. The modelled Weaire-Phelan unit cell and the structure [16]

To determine the accuracy of the CAD model its properties were compared to the properties of the original ALUHAB specimen. Table 4 shows the comparison of the physical properties [16].

Table 4. Comparison of the ALUHAB and the CAD model based on the physical properties [16]

Properties	ALUHAB	CAD model	Difference (%)
Mass (g)	6.6	6.901	4.560
Porosity (%)	89.27	86.43	3.181
Volume (mm^3)	2389	2421	1.339

It can be seen from Table 4, that the difference is less than 5% so the model accurately approximates the physical properties of the original specimen.

2.5. Finite element analysis of the foam structures

Both computational models were analysed using the commercial finite element software SIEMENS Femap with NX Nastran solver for quasi-static loading. The computational models were prepared to represent the experimental setup, and each consisted of an aluminium foam specimen and two rigid plates. Frictionless contact was assumed and used in the model. The rigid top plate had a prescribed displacement, and the bottom plate was fixed and used to measure the reaction force. The aluminium foam specimens were meshed with tetrahedron elements, and material properties were determined using experiments. The model and the results of the ALUFOAM specimen can be seen in Figure 7 [2].

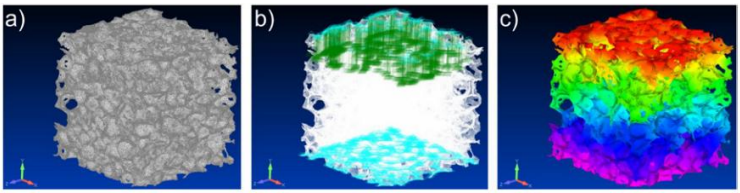

Figure 7. The meshed model (a), the boundary conditions (b), and the displacement state of a foam specimen (c) [2]

The finite element calculations correlated with the experimental results, as shown in Figure 8. For design purposes, the specification of the elastic behaviour of metal foam structural parts is indispensable. The finite element model can describe this feature based on the accurate geometrical reconstruction [2].

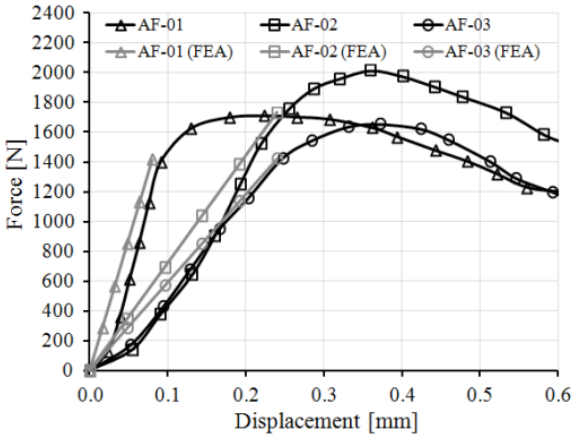

Figure 8. The real and the simulated force-displacement curves of the aluminium foam under quasi-static load [2]

The established CAD model built from Weaire-Phelan unit cells was cut into a quarter model with one layer of unit cells, to prepare it for the finite element simulations, which can be seen in Figure 9. The Young's modulus was set to 2374 MPa and the Poisson ratio to 0.29, respectively [16].

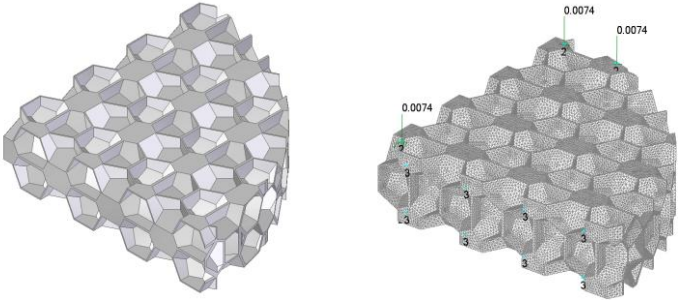

Figure 9. The quarter model and the meshed model

During the evaluation of the finite element results, the force values were in focus. The simulation was conducted

by compressing the specimen. Since a one-layer quarter model was used, this force value was multiplied by 4 and the displacement was scaled up to reflect the 0.06 mm compression of the whole specimen [16]. The evaluated results can be seen in Table 5.

Table 5. The results of the finite element simulation and the laboratory measurement [16]

Property	FEA	Measurement	Difference (%)
Maximum force (N)	170.2	162.6	4.674

From the measurement and the simulation, a force-displacement curve was also evaluated [16], which can be seen in Figure 10.

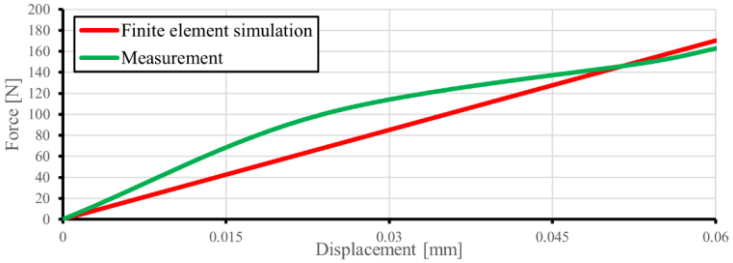

Figure 10. The force-displacement curves of the measurement and the simulation [16]

It is visible from Table 5, that less than 5% relative error was determined so the Weaire-Phelan unit cells and the applied finite element technique can simulate the elastic behaviour of closed cell aluminium foam accurately [16].

2.6. Conclusions

For the numerical determination of the elastic behaviour of ALUFOAM, a manual geometrical reconstruction procedure

was presented. This process was realized in several custom parameterized steps and resulted in a more accurate model than the generally used automatic reconstruction. The difference between the two procedures was proved with comparison analysis. The original image stack was transformed into a form that is suitable for finite element simulations. The finite element calculations correlated with the experimental results and the numerical model precisely described the elastic behaviour of the investigated foam based on the accurate geometrical reconstruction. The procedure can support the design process of load-bearing metal foam parts [2].

The structure of the ALUHAB was approximated by Weaire-Phelan unit cells, which were then multiplied and shaped to match the starting foam specimen. The created CAD model was then simplified into a one-layer quarter model, to prepare it for the finite element simulations. Before the simulations, the CAD model was validated by comparing its physical properties to the original specimen. The comparison has shown that the Weaire-Phelan unit cell structure can model the physical properties of the material with significant accuracy, as the difference values have been less than 5% in all cases. After the validation, the finite element simulations were performed on the simplified model. The boundary conditions and the load were given to recreate the laboratory conditions as closely as possible. The simulation results were compared to the measured data. The use of the Weaire-Phelan unit cell can shorten the design process of structures using metal foam materials, as the creation of the structure only requires the multiplication of one unit cell while being able to model the physical properties and the mechanical behaviour of these materials with sufficient accuracy [16].

3. Finite element analysis of additively manufactured titanium lattice structures

3.1. Brief overview of the research

The demand for patient-specific implants is increasing nowadays and they are getting more and more emphasis in medical engineering developments. The number of standard-sized and bulk hip implant replacements is constantly increasing due to the fact that e.g. the implant was not able to properly integrate into the body. Cellular structures inspired by nature are beneficial for implant purposes in several ways. For example, it is less rigid than a bulk implant and can be optimized for the stiffness of the bone. The other is that the correctly chosen cellular structure (size and shape) facilitates bone ingrowth and osseointegration. Previously, the use of cellular or lattice structures for orthopedic purposes - aware of its advantages - was not possible due to the limitations and possibilities of manufacturing technology. Today, there are industrial solutions for the additive manufacturing (AM) of biocompatible metals (e.g. titanium). One of the greatest advantages of additive technology is that the design engineer is not limited in terms of geometrical design, so even extremely complex structures (e.g. lattice structure) can be realized with high precision. The research thus aims at the design and characterization of cellular titanium structures for hip implants according to medical guidelines and manufactured with additive technology.

Hip implant surgeries and replacements have been increasing over the years, especially for people over 60 years old, for whom it was expected to double over the 2020-2050 range [20]. A review of hip implant revision surgeries over a 6-year time period was performed in [21]. In the study 51.9% of the cause of failure was aseptic

loosening and 16.9% of the cause of instability was reported.

The mechanical properties of the implants should match those of the bone under loading during the activities of daily living. The elastic modulus of bone varies in range from 4 to 30 GPa according to the type of bone [22], hence, the material replacing the bone is expected to have a close value in that range. This requirement can be achieved using implants built from lattice structures. In the case of stiffer implant material, the implant will absorb the whole stress, causing bone resorption around the implant area which leads to the loosening of the implant [23], commonly known as the stress-shielding effect [24].

Lattice structures can be explained as three-dimensional structures composed in topological order and composed of one or more repeated unit cells [25,26]. The effective mechanical properties of such structures can be changed by adjusting parameters to show better properties than those of the original material. In the biomedical field, lattice structures are good solutions to diminish the stiffness of the metal prosthesis and get it as close as possible to the stiffness of the bone [27], thus avoiding the stress shielding effect [28]. Since the lattice structure achieves a high surface area-to-volume range, it facilitates better osseointegration too [29].

These types of lattice structures cannot be manufactured using the traditional way. AM overcomes these manufacturing technology limitations and since it can also handle biocompatible material (e.g. titanium alloys), the solution is in the hands of the design engineer.

Many AM techniques have been researched to choose a good manufacturing technique that suits the properties of titanium alloys. Power bed fusion (PBF) techniques—such as selective laser melting (SLM) electron-beam melting (EBM), and direct metal laser sintering (DMLS)—are

preferable with titanium alloys due to their high-quality direct near-net-shape fabrication [30]. For AM technology the DMLS is used, which applies a Yb (ytterbium)-fiber laser that melts a powdered metal to build a complex structure layer by layer [31].
At the University of Debrecen, research has been going on regarding the development of hip implants, in which I have been involved for several years. A 3D printer working with DMLS technology was procured at the University of Debrecen, which was optimized for Ti6Al4V titanium alloy. Thanks to this, experimental production could begin. The group under my supervision deals with the characterization of different lattice structures, so finite element simulations can be performed based on experiments to determine the material response of the developed structures.

3.2. Introduction of the investigated structures

Ti6Al4V metallic powder (EOS GmbH, Electro Optical Systems, Munich, Germany) with an average particle size of 20–80 μm were utilized for manufacturing the specimens. The nominal chemical composition of the raw material is listed in Table 6.

Table 6. Nominal chemical composition of Ti6Al4V [32]

Element	Data
Ti (wt%)	88-90
Al (wt%)	5.5-6.5
V (wt%)	3.5-4.5
other (wt%)	1

For determining the Young's modulus of the raw material 3 cylindrical specimens were manufactured by an EOS M290

(EOS GmbH, Electro Optical Systems, Munich, Germany) 3D printer with a diameter of 7.5 mm and a height of 15 mm. The machine uses a laser of type Yb fiber with 400 W power. The focus diameter is 100 μm and the scanning speed is 7 ms^{-1} [33]. EOSPRINT 2 software was used in the machine to process the CAD data.
The specimen was then compressed using the INSTRON 8801 servo-hydraulic testing machine. The compression speed was set at 1 mm/min. A video extensometer provided with a heavy-duty camera was used to detect the displacement along the compression process [34]. The Young's modulus of the raw material was determined and used in the later finite element simulations are listed in Table 7. The standard deviaton for the measured Young's modulus was 1.878. The Poisson's ratio of the material is 0.34 [32].

Table 7. Young's modulus of the raw material [32,34]

Property	Data	Measured data
Young's modulus (GPa)	113.8	106.24

A difference of 7.1% was noticed for Young's modulus given by the producer [32] for the Ti6Al4V titanium alloy. This could be due to the following reasons: printing accuracy and quality, material quality or measurement error [34].
According to medical guidelines, implants designed with open cell or lattice structures greatly helps bone ingrowth and osseointegration. Considering that these structures are produced by additive manufacturing, the design engineer has freedom in terms of geometric design during the process. The choice was limited to 4 lattice structure types: 3D lattice infill pattern (3DLIP); double-pyramid lattice with cross (DPLC); double-pyramid lattice and face

diagonals (DPLFD); Octahedral lattice (OL), see in Figure 11.

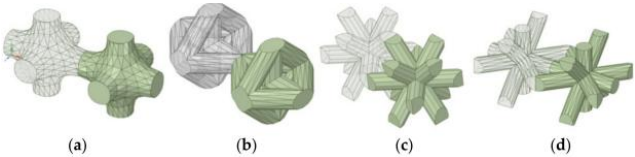

Figure 11. The lattice structures: (a) 3DLIP; (b) DPLC; (c) DPLFD; (d) OL [35]

The geometrical parameters of the lattice structures can be adjusted, so the porosity of the designed structures was set to be the same as possible so that the results of the mechanical tests can be compared. These lattice structures are available in SpaceClaim within the ANSYS software 2021 R2. The dimensions of the specimens that are the subject of the test are 20 mm × 20 mm × 30 mm. A bulk part was designed with a height of 5-5 mm at the top and bottom of the test specimen to ensure the possibility of the most accurate measurement. Since the parameters of the lattice structures can be customized, the structures were designed considering the ISO 13314 standard [19] and in such a way as to have approximately the same porosity for comparability. The models and the specimens can be seen in Figure 12 and those parameters are listed in Table 8.

Table 8. The main parameters of the specimens [35]

Lattice type	Porosity (%)	Volume (mm^3)
3DLIP	74	2079.17
DPLC	74	2067.58
DPLFD	71	2313.96
OL	70	2431.76

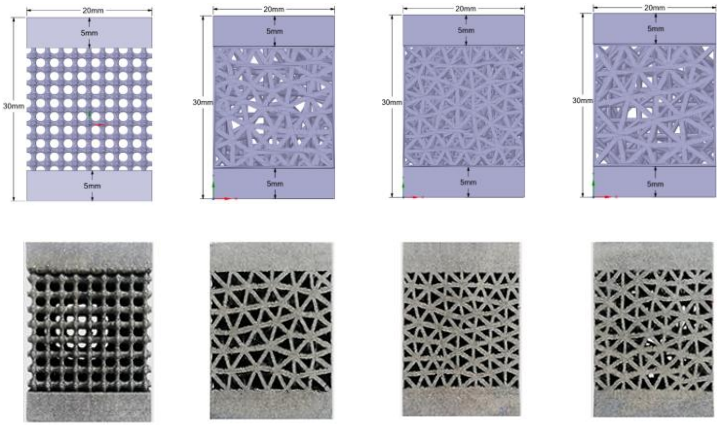

(a) (b) (c) (d)

Figure 12. The specimens manufactured via 3D printer: (a) 3DLIP; (b) DPLC; (c) DPLFD; (d) OL [35]

The specimens were manufactured by the EOS M290 (EOS GmbH, Electro Optical Systems, Munich, Germany) 3D printer.

The dimensional accuracy of the specimens can have a great impact on the results of the laboratory measurement. Therefore an extensive investigation in terms of geometric and shape accuracy was carried out using a 3D scanner [36]. During the investigation, the designed CAD models with the test specimens manufactured with the 3D printer were compared. The manufacturing accuracy - in addition to other findings - was found to be suitable for the subsequent tests.

3.3. Compression tests

An INSTRON 8801 Servohydraulic Fatigue Testing Machine (INSTRON, Norwood, MA, USA) was used to conduct the compression tests. An INSTRON (INSTRON, Norwood, MA,

USA) AVE2 video extensometer with an accuracy of 0.5% was used with the compression test to obtain an accurate measurement of the displacement during the experiment. The test was done at room temperature [35]. The test setup can be seen in Figure 13.

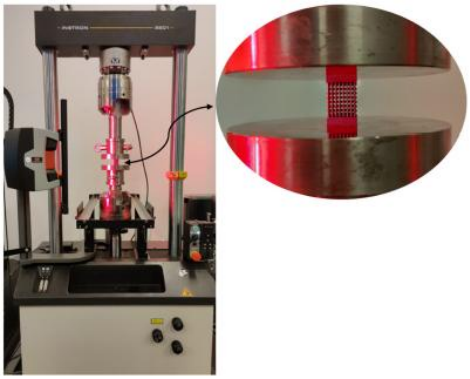

Figure 13. Test setup for the compression of lattice structures [35]

The experiments were conducted according to displacement at a constant rate, set to 1 mm/min. A maximum force of 15 kN was applied to each specimen. No lubrication was used. Three samples of each lattice structure were tested under compression [35].
The results of the compression tests were evaluated for each set of specimens. From the stress-strain curves the effective Young's modulus (E_{eff}) of the different lattice structures were calculated, see in Table 9.
The compression test was considered in the elastic zone and the results were shown up to 0.004 strain. The average stress-strain curves of different lattice structures are shown in Figure 14.

Table 9. Results of the compression test [35]

Lattice type		E_{eff} (MPa)
3DLIP	1	8702
	2	9298
	3	8030
	average	8676.7
	standard deviation	634.3
DPLC	1	7741.5
	2	7565.4
	3	7896.9
	average	7734.6
	standard deviation	165.8
DPLFD	1	8375
	2	8620
	3	8101.3
	average	8365.4
	standard deviation	259.5
OL	1	11688
	2	10742
	3	10239
	average	10889.7
	standard deviation	735.7

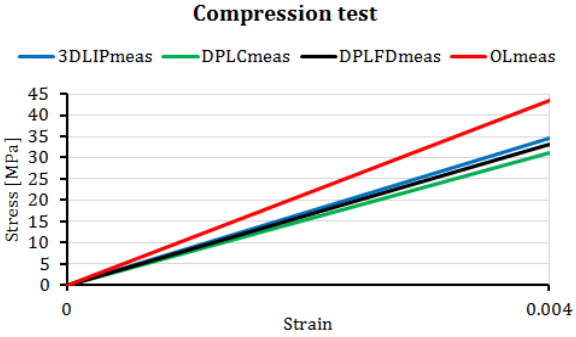

Figure 14. Average stress-strain curves of the different lattice structures [35]

3.4. Finite element analysis of the cellular titanium structures

The numerical simulation of the compression test using the same boundary conditions was performed using the ANSYS R2 Workbench. The experiences of previous works [37,38] were also taken into consideration during the establishment of the finite element model. Mesh sensitivity analysis was also done [35] to find the optimal element size. The finite element models of the different lattice structures can be seen in Figure 15.

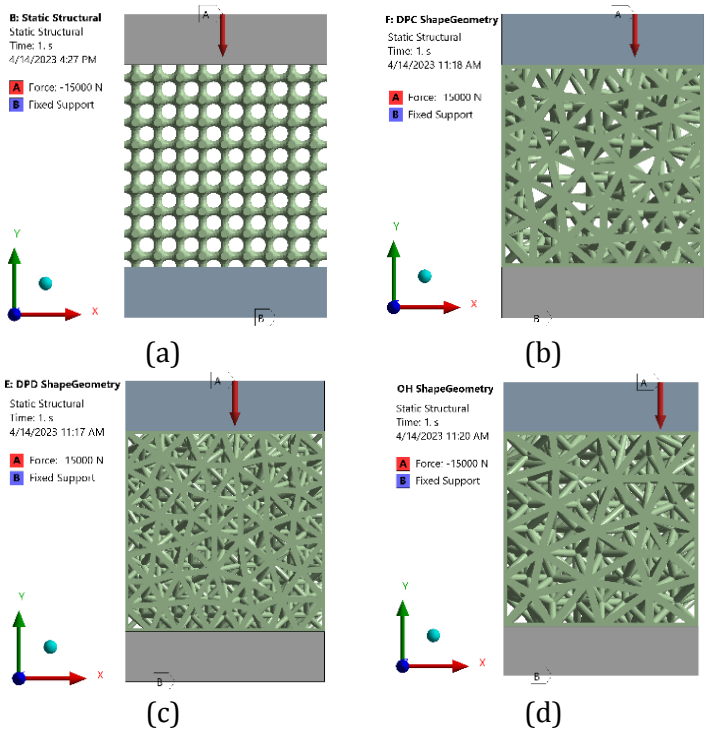

Figure 15. Finite element models of the lattice structures: (a) 3DLIP; (b) DPLC; (c) DPLFD; (d) OL [35]

Stress-strain curves were generated from the finite element simulation runs and the effective Young's modulus was determined and than compared with the results of the compression test, see Figure 16 and Table 10.

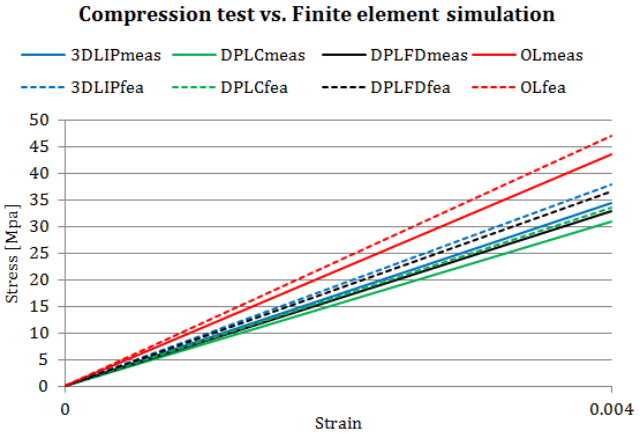

Figure 16. Stress-strain curves of different lattice structures [35]

Table 10. Effective Young's modulus determined from the compression test and the numerical simulation [35]

Lattice type	E_{eff} (MPa)		Percentage difference (%)
	measurement	simulation	
3DLIP	8676.7	9592.9	9.6
DPLC	7734.6	8356.4	7.4
DPLFD	8365.4	9260.1	9.7
OL	10889.7	11719	7.1

3.5. Conclusions

The most commonly used hip implants typically have a bulk structure, which does not take into account the operating environment from a mechanical point of view.

Lattice structures provide a good basis for the design of structures with strength similar to bone, and nowadays the production of this complicated structure is also solved.
Considering the medical guidelines, 4 types of lattice structures (3D lattice infill pattern; double-pyramid lattice with cross; double-pyramid lattice and face diagonals; octahedral lattice) from Ti6Al4V titanium alloy with the same porosity were designed, from which the specimens were manufactured using direct metal laser sintering technology. Compression tests were performed under laboratory conditions, from which the effective Young's modulus of these structures was determined.
To be able to design the hip implant part designed from the lattice structure with numerical tests during the design, finite element simulations were performed, which showed a good agreement with the laboratory measurements, thereby validating our finite element models.
With the help of the above listed investigations, it was possible to determine the material response of the specimens made of lattice structures, which is a good starting point for the design of patient-specific hip implants.

4. Shape optimization of axisymmetric rubber parts

4.1. Brief overview of the research

Designing the suspension systems of vehicles is a demanding engineering task. Currently, driving stability is ensured by electronically controlled active suspension systems. The objectives set in the course of designing include improving travel comfort, decreasing the dynamic loading of the wheels and decreasing the suspension workspace [39,40]. Similar possibilities are offered by the use of air springs.

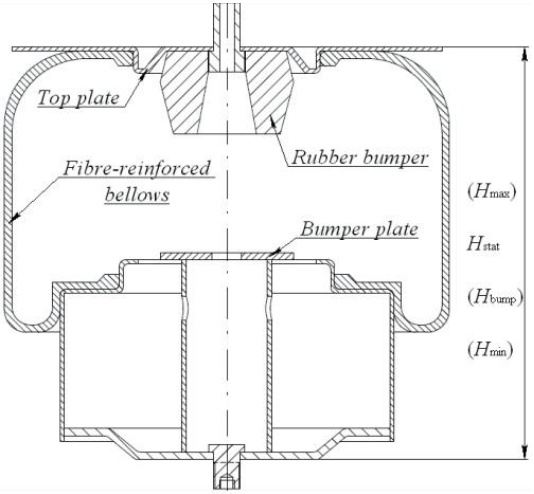

Figure 17. The air spring [40]

The rubber bumpers (see Figure 17) built into the air springs of buses perform several crucial functions, such as working together with the air spring as a secondary spring, thus modifying the original characteristics of the air spring

when pressed together (characteristics of the dotted and dashed lines in Figure 18) [40].

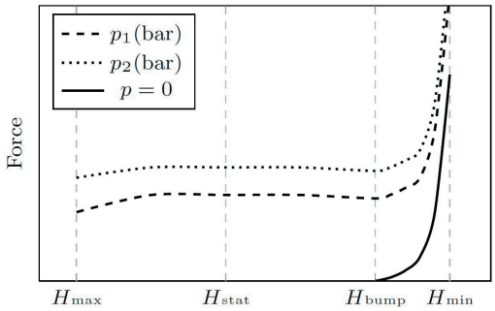

Figure 18. The "lift" diagram [40]

When the bus is in a stationary position and settles to the ground, the static weight of the chassis and the body rests on the bumper; in this case, the solid line characteristic is active. If the fibre-reinforced bellows of the air spring wears through while the bus is running, the vehicle can safely reach the nearest garage at a limited speed while bouncing on the bumper; no additional damage will occur. It prevents metal-on-metal collision at large dynamic impulses and absorbs the impulse. These rubber bumpers are subject to compressive stress, for which the characteristics show a progressive feature [40].

It is a fundamental requirement that they should have a specified load-displacement curve under load; setting this objective results in a shape optimization task. The optimization aims to achieve a specified characteristic through the geometric design of the rubber bumper while the material characteristics remain the same [40].

Several authors have formulated shape optimization for the specified stiffness of rubber parts, in which the analysis was done using commercial finite element software or a

finite element code of their development [41-44]. Rubber products can suffer from large deformation upon working conditions while behaving as a non-linearly elastic, isotropic and incompressible material. This kind of behaviour of rubbers can be described with a hyperelastic material model, which uses the strain energy to describe the relationship between stress and strain considering the related continuum mechanics background. Such hyperelastic material models are Mooney-Rivlin, Ogden, Yeoh, etc. [45].

In solving the shape optimization problem the usage of artificial intelligence (AI) tools was an important aspect. AI methods include, among others, the optimization algorithms inspired by nature (Genetic Algorithm, Differential Evolution, Simulated Annealing, etc.) or machine learning procedures (Neural Networks, Deep Learning, Support Vector Regression, etc.) [46].

The research intends to determine the behaviour of rubber bumpers in the complete range of operation, and thus the shape optimization aims to achieve the specified spring characteristics. Since there is no active control in the rubber bumpers, shape optimization may provide the required load-displacement curve. In connection with the objective set, achieving the aim of the optimization will require an efficient force-displacement calculation, which is performed using the finite element method [40]. This goal was served by a finite element program developed for the investigation of axisymmetric rubber parts and a commercial finite element software as well, which can be conveniently fit to the shape optimization procedure. However, a series of finite element runs of non-linear problems are time-consuming, therefore Support Vector Regression (SVR) as a surrogate model was used to replace the costly engineering simulations and to support the optimizations. In this thesis, two shape optimization

methods of axisymmetric rubber bumpers are introduced. The novel optimization procedures developed are suitable for the shape optimization of rubber bumpers with specified characteristics. The efficiency of the methods was verified by examples.

4.2. Material model of the investigated rubbers

Rubber bumpers may undergo large deformations under load, which in itself shows non-linear behaviour. The changing contact range between the parts and the incompressibility of the rubber increases this nonlinear behaviour further [40].

A successful finite element simulation of rubber parts hinges on the selection of an appropriate strain energy function and the accurate determination of material constants [47]. For rubbers, the material models are generally given by the strain energy density function [45]. The strain energy density function of nearly incompressible materials can be divided into a volume-preserving and a volume-changing part

$$W = W_D(\boldsymbol{C}) + U(J), \qquad (1)$$

where $W_D(\boldsymbol{C})$ is the volume preserving part of the strain energy density and $U(J)$ is the strain energy density part resulting from the volume change. $\boldsymbol{C}$ is the volume preserving member of the right Cauchy-Green strain tensor, while J is the Jacobian [40].

Several material models can be found in the literature for the volume-preserving part of strain energy density. Measurements of the rubber material are needed to determine the material constants used for finite element analysis. The main load of the rubber bumper is compression, therefore compression tests according to the

ISO 7743 standard [48] and the related curve-fitting processes were performed on rubber specimens and products [49, 50]. As a result of extensive research, it was found, that the two-term Mooney-Rivlin hyperelastic material model is suitable for the numerical calculations. The strain energy density function for the two-term Mooney-Rivlin model is

$$W_{MR} = c_{10}(I_1 - 3) + c_{01}(I_2 - 3) + \frac{1}{2}\kappa(J-1)^2, \quad (2)$$

where I_1 and I_2 are the first and second scalar invariants of $\boldsymbol{C}$, respectively. The c_{10} and c_{01} are the Mooney-Rivlin material constants, while κ is the bulk modulus.

4.3. Shape optimization of rubber bumper using SVR

The meridian section of the investigated axisymmetric rubber bumper can be seen in Figure 19.

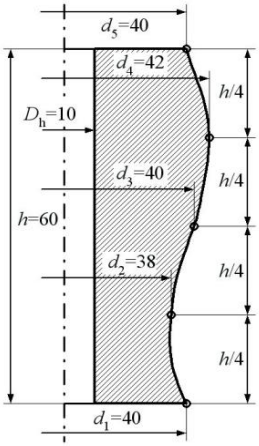

Figure 19. Meridian section of the investigated bumper (the dimensions are in mm) [40]

The outer skirt of the bumper is described using a cubic spline in five control points. The rubber bumper is subjected to a prescribed 20mm displacement.

4.3.1. Finite element model of the rubber bumper

To establish the force-displacement curve under compression a special purpose finite element code was developed using the so called combined technique, which is based on the following functional

$$\pi(\boldsymbol{u},\bar{J},\bar{p}) = \int_V W_D(\boldsymbol{C})\,dV + \int_V U(\bar{J})dV + \int_V p(J-\bar{J})\,dV + \frac{1}{2}\int_{A_c} c g_n^2\,dA - \pi_{ext}(\boldsymbol{u}), \tag{3}$$

where the displacement field $\boldsymbol{u}$ is approximated using the quadratic tensor product space, the volume change $\bar{J}$ and the hydrostatic pressure $\bar{p}$ are approximated using linear functions independently of each other. $U(\bar{J})$ is the penalty parameter member, J can be indirectly derived from the displacement and is independent of $\bar{J}$, c is the penalty parameter of the contact, g_n is the gap function, $\pi_{ext}(\boldsymbol{u})$ is the potential of the external forces, V is the volume of the rubber and A_c is the contact surface [40]. To discretize the functional nine-node iso-parametric axisymmetric finite elements are used. Applying the Total-Lagrange description to the variation equations of (3) according to $\boldsymbol{u},\bar{J},\bar{p}$ [45], after finite element discretization, and the Newton-Raphson iteration [51] is finally obtained

$$\mathbf{K}_T\Delta\mathbf{u} = \Delta\mathbf{f}, \tag{4}$$

where $\mathbf{K}_T$ is the structural tangent stiffness matrix, $\Delta\mathbf{u}$ is the vector of nodal point displacement increment and $\Delta\mathbf{f}$ is the unbalanced load vector. The validation and calibration of the program (mesh, material constants and finite element input data) were performed according to [52]. For the finite element code, a data generation program (mesh, boundary conditions, loads and finite element input data) has also been developed [40].
The finite element input data are given in Table 11, the original and the deformed shape of the bumper, furthermore the initial force-displacement curve calculated by the finite element code can be seen in Figure 20.

Table 11. Finite element input data [40]

Properties	Data
c_{10} Mooney-Rivlin constant (N/mm²)	0.5
c_{01} Mooney-Rivlin constant (N/mm²)	0.125
κ bulk modulus (N/mm²)	1000
Δu prescribed displacement (mm)	2
Number of load steps	10

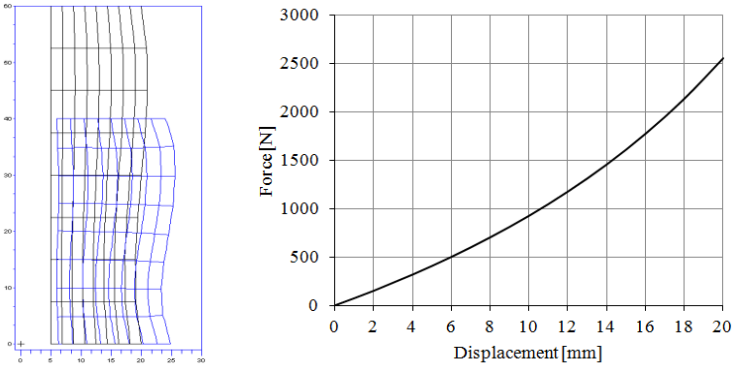

Figure 20. The initial and deformed shape of the bumper and the force-displacement curve [40]

4.3.2. The optimization method

In both optimization processes, we start from the force-displacement curve of an existing construction. The optimization aims to minimize the difference between the initial force-displacement curve and the desired force-displacement curve, see Figure 21.

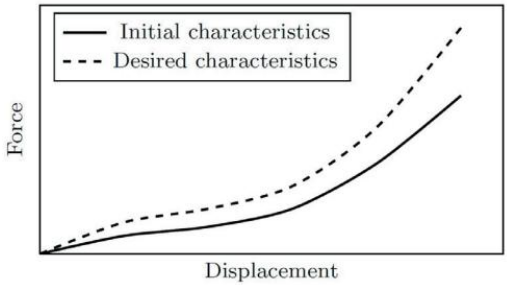

Figure 21. Working characteristics of a rubber bumper with optimum shape and initial shape [40]

The objective function of the shape optimization problem can be formulated in several ways. In the first case, the objective function gives the area between the desired force-displacement curve and the curve obtained by finite element computation for a specific rubber bumper shape

$$\Delta W(\boldsymbol{d}) = \int_0^{s_0} \left| F_{opt}(s) - F_{FEA,\boldsymbol{d}}(s) \right| ds, \qquad (5)$$

where ΔW is considered on $\Omega \in \mathbb{R}^n$, the set of possible design parameter vectors is $\boldsymbol{d}$, s_0 is the limit of the operation range, F_{opt} and $F_{FEA,\boldsymbol{d}}$ denote the compressive force of the desired characteristics and the compressive

force calculated by the finite element method for a specific geometry (determined by $\boldsymbol{d}$), respectively [40]. The optimization range Ω is given by inequality geometric constraints from technology limitations, and n is the number of the design parameters. Function ΔW has to be minimized by determining the optimum design parameter vector $\boldsymbol{d}_{opt}$, that is

$$\Delta W(\boldsymbol{d}_{opt}) = \min_{\boldsymbol{d}\in\Omega} \Delta W(\boldsymbol{d}). \tag{6}$$

Since numerical methods are used, the process results in an approximate value of the optimum [40].

The first step of the process is to solve a non-linear regression problem for function ΔW. The regression procedure is based on the learning points $(\boldsymbol{d}_i, \Delta W(\boldsymbol{d}_i)) \in \mathbb{R}^{n+1}, i = 1, \dots, N$, where N is the number of learning points and $\Delta W(\boldsymbol{d}_i)$ are calculated with finite element simulations.

The SVR model proposed by [53] is used to find the regression function. The application of SVR in non-linear models has the advantage that the transformation function between the input space and the feature space can be hidden [54], and machine learning procedures can be applied to find an appropriate regression function. The calculations are carried out with the SVR package of "R" software. Since the values of the regression function provided by the software are available for arbitrary design parameter vectors in Ω, the place of the minimum of ΔW, i.e. the value of the optimum design parameter vector, can be determined numerically. The theoretical background of the method is summarized in [40].

Using the finite element method, the values of ΔW are determined for the design parameters $d_1, \dots, d_N \in \Omega$ and the learning points play the role of the given data points in the non-linear regression procedure. Based on the

research [53] ε-intensive error function is applied, where the ε may be regarded as the parameter controlling the smoothness of the solution. When using regression models, we have to take into consideration that certain learning points will disturb the run of the regression function [40]. These effects are moderated using slack variables [53] and a hyper-parameter C is introduced, which can be regarded as a penalty parameter that penalizes excessive divergence. In the SVR model, the so-called kernel functions play a central role. By choosing a suitable kernel function, an appropriate solution to the regression problem can be achieved [40]. In this optimization problem the Gaussian kernel function is chosen

$$k_i(\boldsymbol{d}) = e^{-\gamma\|\boldsymbol{d}-\boldsymbol{d}_i\|}, \tag{7}$$

where γ is a hyper-parameter controlling the form of the kernel functions. The value of the regression function is fundamentally determined by the learning points. The regression function obtained from the SVR model is denoted by ΔW_{SVR} [40]. The accuracy of the regression provided by the SVR model depends on γ and C. An optimum choice of hyper-parameters leads to the error of the learning process

$$\delta_1 = \sqrt{\frac{\sum_{i=1}^{N}(\Delta W_{FEA}(\boldsymbol{d}_i) - \Delta W_{SVR}(\boldsymbol{d}_i))^2}{\sum_{i=1}^{N}(\Delta W_{FEA}(\boldsymbol{d}_i))^2}} \leq \delta_1^*, \tag{8}$$

where $\Delta W_{FEA}(\boldsymbol{d}_i)$ are the values of the objective function determined by the finite element calculations. δ_1^* can be specified by the user according to the expected accuracy [40]. The learning points are used to test the error δ_1 of the regression function produced by the software optimizing the hyper-parameters γ and C. If the error δ_1 is within the

specified limit δ_1^* the regression function is accepted and is used for further calculation [40].
Considering a set

$$D = \{d_1, \dots, d_P\} \subset \Omega, \tag{9}$$

according to technology limitations the minimum of ΔW_{SVR} on D is determined numerically, where P is the number of possible solutions.
The finite element calculation is performed with the optimum design parameter vector determined using SVR and the condition

$$\delta_2 = \frac{\left|\Delta W_{FEA}(\boldsymbol{d}_{opt}) - \Delta W_{SVR}(\boldsymbol{d}_{opt})\right|}{\Delta W_{FEA}(\boldsymbol{d}_{opt})} \leq \delta_2^* \tag{10}$$

is checked, where the limit δ_2^* is specified by the user. If (10) is fulfilled, the optimization is considered to be completed [40].

4.3.3. Numerical example

The geometry of the rubber bumper was introduced in Figure 19. The outer skirt of the bumper is described using a cubic spline in five control points. These control points are the design parameters [40]. The initial and the desired characteristics can be seen in Figure 22.

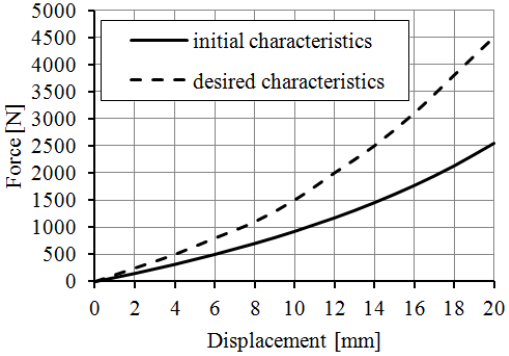

Figure 22. The initial and desired force-displacement curves [40]

In the investigation the design parameters in [mm] are defined according to the following conditions:

$$\boldsymbol{d} = (d_1, d_2, d_3, d_4, d_5), \text{ where } \begin{cases} d_1 \epsilon [40,56] \\ d_2 \epsilon [d_1 - 4, d_1 + 4] \\ d_3 \epsilon [d_2 - 2, d_2 + 2] \\ d_4 \epsilon [d_3 - 2, d_3 + 2] \\ d_5 \epsilon [d_4 - 2, d_4 + 2] \end{cases}$$

and d_1, d_2, d_3, d_4, d_5 are even numbers [40].
Under the specified accuracy, the number of possible solutions is $P = 1215$. The number of learning points is $N = 10$. During the optimization process, the following values were set: $\varepsilon = 0.01, \delta_1^* = 0.02, \delta_2^* = 0.05$, while the optimum hyper-parameters were found $\gamma = 0.1, C = 20$, where $\delta_1 = 0.013$. The goodness of learning is shown in Figure 23.

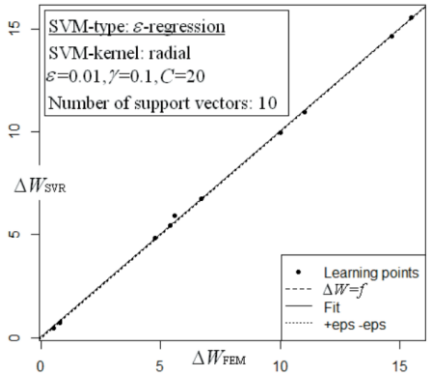

Figure 23. SVR best fit [40]

Based on the calculation, the minimum work difference of the possible solutions is $\Delta W_{SVR}(\boldsymbol{d}_{opt}) = 0.432$Nm, for which the optimum design parameters are $\boldsymbol{d}_{opt} =$ (52,48,54,54,54) in mm. The deformed shape of the optimal geometry and the characteristics obtained for the control finite element calculation run for the optimum design parameters can be seen in Figure 24. The $\Delta W_{FEA}(\boldsymbol{d}_{opt}) = 0.412$Nm, so the tolerance is $\delta_2^* = 0.048$ [40].

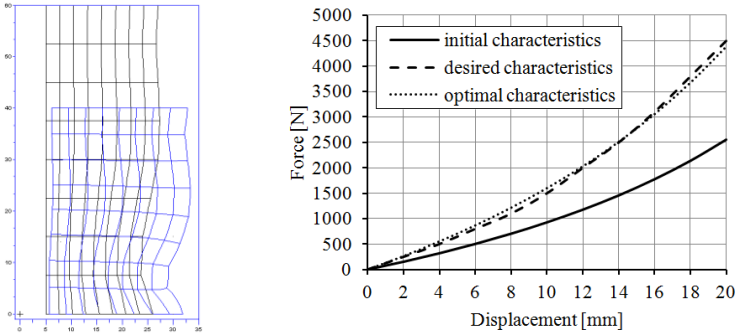

Figure 24. The deformed shape of the optimal geometry and the optimal force-displacement curve [40]

4.4. Shape optimization of rubber bumper using local search algorithm powered by SVR

As a second example another axisymmetric rubber was investigated, the meridian section of the part can be seen in Figure 25.

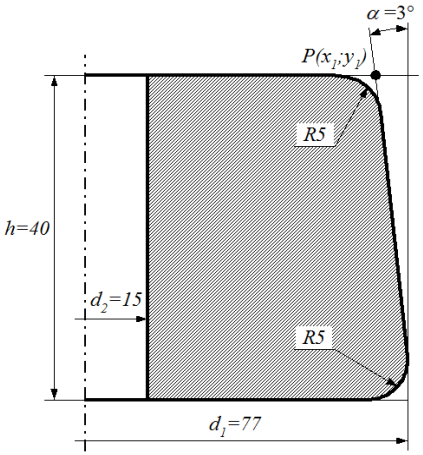

Figure 25. Meridian section of the investigated bumper (the dimensions are in mm) [47]

4.4.1. Finite element model of the rubber bumper

The main load of the rubber bumper is compression, therefore a compression test and curve-fitting process were performed on rubber specimens according to [49,50]. For the finite element calculations the Femap Siemens commercial finite element software was used. The boundary conditions are axisymmetric, so linear isoparametric quadrilateral elements were applied and the size of the element was 1mm. Since the rubber bumper comes into contact on the bottom and top with flat steel

plates, frictional contact was defined between the surfaces. The coefficient of static friction was selected according to [55]. The rubber bumper is subjected to a prescribed 12mm displacement.
The finite element input data are given in Table 12., the deformed shape of the bumper, furthermore the initial force-displacement curve calculated by the finite element software can be seen in Figure 26.

Table 12. Finite element input data [47]

Properties	Data
c_{10} Mooney-Rivlin constant [N/mm²]	1.28801
c_{01} Mooney-Rivlin constant [N/mm²]	1.1371
κ bulk modulus [N/mm²]	1000
μ friction coefficient	0.6

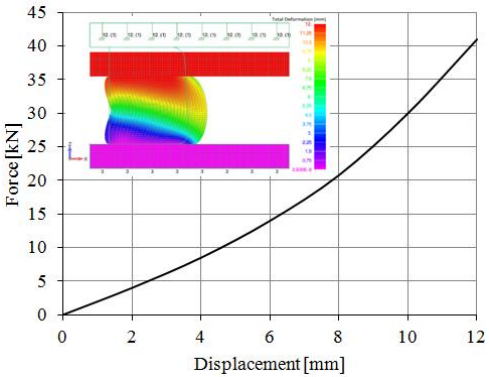

Figure 26. The deformed shape of the bumper and the force-displacement curve [47]

4.4.2. The shape optimization method

In the second problem, the objective function is an error value and was calculated as the sum of the square error

$$E(\boldsymbol{d})_{FEA} = \sum_{i=1}^{10} \left(F_i(\boldsymbol{d}_{opt}) - F_i(\boldsymbol{d})\right)^2, \tag{11}$$

where $E(\boldsymbol{d})_{FEA}$ is the error value in an investigated design point, $F_i(\boldsymbol{d}_{opt})$ is the ith results of the required compressive force value in the optimal design point and $F_i(\boldsymbol{d})$ is the ith results of the required compressive force value in the initial design point [47]. The finite element analysis was solved in 100 steps with every 10th step created as output. $E(\boldsymbol{d})$ is considered on $\Omega \in \mathbb{R}^n$ and has to be minimized by determining the optimum design parameter vector $\boldsymbol{d}_{opt}$, that is

$$E(\boldsymbol{d}_{opt}) = \min_{\boldsymbol{d} \in \Omega} E(\boldsymbol{d}). \tag{12}$$

The efficient calculation of the objective function naturally requires sufficiently accurate finite element calculations, therefore the appropriate finite element model plays a central role. In this research, the local stochastic search method is used to find the global optimum using finite element calculations. Due to the nature of the local stochastic search procedure, it requires many finite element calculations, which are extremely time-consuming. It can be explained by that an appropriately high number of iterations are needed to find the acceptable environment of the global optimum. To accelerate the finite element model, pre- and postprocessing were automated with the use of Visual Basic for Applications (VBA), which allowed to directly access the Femap from Excel. The finite element model was controlled with a macro running in Excel and $E(\boldsymbol{d})_{FEA}$ values were determined for each sample [47]. Thanks to this

automation the local stochastic search algorithm was implemented and run for the shape optimization task. The success of the optimization depends on the correct choice of the parameters of the local search algorithm. The calculation of the finite element model is in itself time-consuming, which makes it impossible to investigate the local search algorithm parameters [47].

The novelty of the research was that a trained SVR surrogate model was integrated into the size selecting process of the search space of the algorithm. Using the stochastic search algorithm and the adjusted parameter, the finite element model was directly run to solve the shape optimization of the rubber bumper [47].

The pseudocode of the local search algorithm is the following [47]:

(1) Select a starting point $\boldsymbol{d}_0 \in \Omega$ randomly;
(2) $\boldsymbol{d}_m \rightarrow \boldsymbol{d}_{m+1}$ - generate a random direction $\boldsymbol{a}_m \in \mathbb{R}^n$, if $\boldsymbol{d}_m + \boldsymbol{a}_m \notin \Omega$ then generate a new $\boldsymbol{a}_m$ direction and repeat it. If $\boldsymbol{d}_m + \boldsymbol{a}_m \in \Omega$ then $\boldsymbol{d}_{new} = \boldsymbol{d}_m + \boldsymbol{a}_m$;
(3) If $E(\boldsymbol{d}_{new})_{SVR} < E(\boldsymbol{d}_m)_{SVR}$, then $\boldsymbol{d}_{m+1} = \boldsymbol{d}_{new}$, otherwise $\boldsymbol{d}_{m+1} = \boldsymbol{d}_m$, further $m = m + 1$;
(4) Stopping criterion - if the maximum iteration number is reached.

To generate $\boldsymbol{a}_m$ direction, a normally distributed random number with zero mean is selected in all directions of the design variables. This algorithm contains two parameters to be determined, which are the σ standard deviation belonging to a random number and m_{max} maximum iteration number should be provided as a precondition of the stopping criterion, meaning the cost of the algorithm. These parameters are involved in the parameter selection process. The program written was operated for running the shape optimization task in an automatized closed system by providing the parameters. As a result, it

determined the optimal objective function value as well as its other relevant values [47].

4.4.3. Numerical example

In this case of the research, the applicability of the local stochastic search algorithm in the optimization process was investigated, therefore the desired characteristics was determined from a predefined optimum shape.
Taking technological considerations into account the height h of the product and the draft angle α were fixed, see Figure 25. The outer diameter d_1 and the hole diameter d_2 were chosen as design parameters. In the shape optimization, the design parameters are defined in [mm], according to the following conditions [47]:

$$\boldsymbol{d} = (d_1, d_2), \text{where} \begin{cases} d_1 \in [70{,}130] \\ d_2 \in [10{,}60] \end{cases} \text{and } x_1 - \frac{d_2}{2} \geq 15,$$

where $x_1 = \frac{d_1}{2} - h \tan \alpha$ is the coordinate of point *P*, see Figure 25.
To test the goodness and efficiency of the proposed method a predefined optimum shape was chosen, where $\boldsymbol{d}_{opt} = (108; 33)$ in mm and $E(\boldsymbol{d})_{FEA} = 0$. For the initial shape $d = (77; 15)$ in mm and $E(\boldsymbol{d})_{FEA} = 7911.2\text{kN}^2$.
To map the values of the objective function a series of finite element calculations were performed with the increment of 5 mm along with the design parameters selected from Ω. It means altogether 128 vertex pairs. Thanks to the above mentioned automation these calculations could be implemented in a closed system. The objective function values on the optimization range by applying the finite element model can be seen in Figure 27.

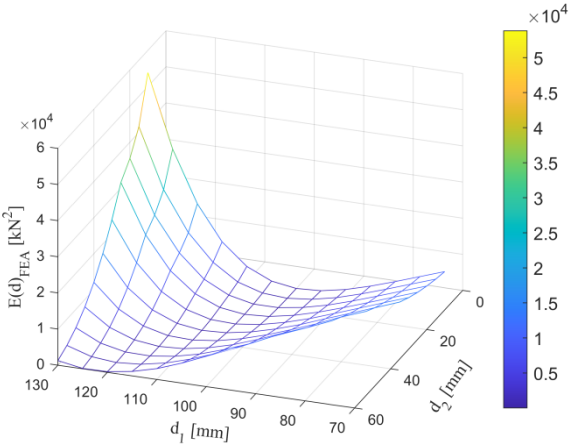

Figure 27. Objective function values on the optimization range by applying the finite element model [47]

The smallest objective function value was at $\boldsymbol{d} = (120; 55)$ in mm, where $E(\boldsymbol{d})_{FEA} = 3.267\text{kN}^2$. It can be seen, that the error value is small compared to the initial shape, however, the determined point is far away from the known optimum [47].

To investigate the local search algorithm, $\sigma = 20\text{mm}$ and $m_{max} = 5000$ values were selected. The search method was run for the two-variable shape optimization task for the rubber bumper. Table 13 contains better function values accepted in m iteration by the algorithm and its related geometric variable values and Figure 28 visualizes the change in the location of the better function accepted by the optimization method. Considering the results, the efficiency of the algorithm was low, as it was not suitable for identifying better value than $E(\boldsymbol{d})_{FEA} = 0.051\text{kN}^2$ even after passing $m = 1250$ iterations. The process could not approach the global optimum even after $m = 5000$ calculation, although it managed to approach it [47].

Table 13. Better function values accepted by the local search algorithm [47]

m	d_1 (mm)	d_2 (mm)	$E(\boldsymbol{d})_{FEA}$ (kN²)
0	89.851	31.215	4828.676
2	109.522	25.262	748.357
4	113.054	44.676	25.124
17	113.506	43.719	1.057
427	111.375	39.416	0.654
514	107.389	31.960	0.267
1250	109.184	35.372	0.051

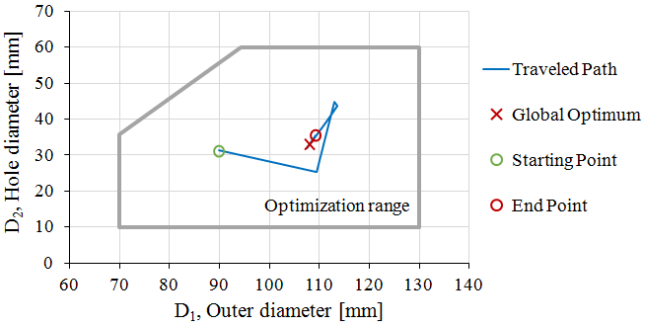

Figure 28. Investigated design parameters by the local search algorithm [47]

The parameters of the local search algorithm have a great influence on the results. As a next step, the parameter selection of the algorithm is done using a trained SVR model. The objective of using SVR is to discover the function $E(\boldsymbol{d})_{SVR}$ that best predicts the value of $E(\boldsymbol{d})_{FEA}$ associated with each value of $\boldsymbol{d}$. 22 learning points were selected from Ω according to [56] and see in Figure 29, then $E(\boldsymbol{d})_{FEA}$ values were determined by the use of finite element analysis. These samples are used as learning points to train the SVR surrogate model with a cubic kernel function. Regression Learner application built into Matlab was used for this purpose and the regression model

training was performed manually [47]. The number of the required learning points was determined in a former research [56].

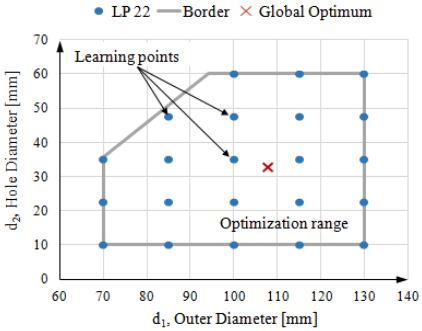

Figure 29. The selection of learning points from the optimization range [47]

For the fitting process, $\varepsilon = 0.001$ and kernel scale=1 values were selected, while the rest of the hyperparameters were set automatically by the Regression Learner application. The predicted response $E(\boldsymbol{d})_{SVR}$ of the SVR model is plotted against the true response $E(\boldsymbol{d})_{FEA}$, see Figure 30 [47].

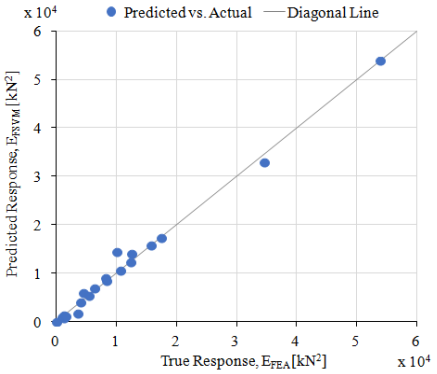

Figure 30. SVR best fit [47]

Using the trained SVR model, predictions were made for each combination of integer values of design parameters. The predicted objective function values are illustrated above the optimization range according to Figure 31. As a result, it seemed suitable for approaching the values of the nonlinear objective function [47].

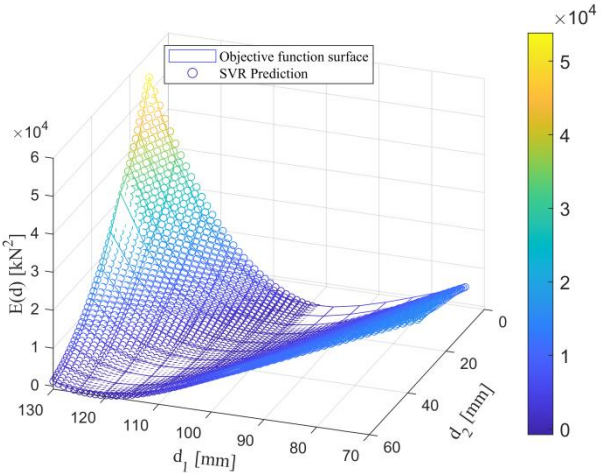

Figure 31. Predicted points for the objective function values by the SVR model in the optimization range [47]

The trained surrogate model was used to find the appropriate parameters (σ and m) of the local search algorithm. The process step by step can be found in [47] and will not be detailed due to lack of space. Based on the research it can be pointed out that no optimal value can be defined for the size of the search space. In the beginning, a large space is needed for mapping the optimization range and avoiding getting stuck in the local optimum. On the other hand, a smaller space is needed in the environment of the global optimum for the algorithm to have a better

chance of finding an optimal solution. Decreasing search space may happen through various functions such as an exponential function or after a manually selected iteration number [47]. The main objective was to decrease σ value if the iteration number exceeded the prescribed value. As a result of extensive investigation adjustment of the parameters by tightening the search space was found to be the most accurate for the optimization. Table 14 shows the parameters of the local search algorithm.

Table 14. Adjustment of local stochastic search algorithm by tightening search space [47]

m_{start} iteration number start	1	2001
m_{stop} iteration number stop	2000	3000
σ (mm) standard deviation	30	0.5

Table 15 includes better function values and their geometry variable values accepted by the algorithm, while Figure 32 visualizes the path done by the algorithm [47].

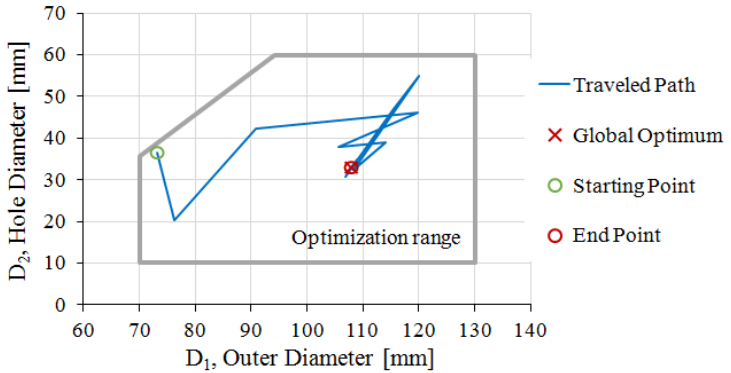

Figure 32. Investigated design parameters by the adjusted local search algorithm [47]

Table 15. Better function values accepted by the adjusted local search algorithm [47]

m	d_1 (mm)	d_2 (mm)	$E(\boldsymbol{d})_{FEA}$ (kN²)
0	73.237	36.540	14624.63333
1	76.240	20.204	9106.38117
2	90.939	42.385	7081.81690
3	119.767	46.106	603.32863
4	105.709	37.932	482.39861
6	114.168	38.937	249.21546
18	108.312	32.409	8.77936
89	119.990	54.945	3.30837
204	115.371	46.689	2.16783
338	109.392	35.507	0.54223
410	106.942	30.752	0.06769
1056	108.970	34.950	0.03469
2073	108.861	34.704	0.03287
2158	108.738	34.448	0.02950
2178	108.562	34.174	0.01972
2202	108.511	34.070	0.01649
2219	108.338	33.685	0.00402
2307	107.900	32.816	0.00258
2373	107.966	32.937	0.00025

The objective function values were equal until three decimals were reached, even when the variables were within one decimal to the known optimum value. The effect of tightening search space coincided with what was experienced with the surrogate model. The optimum found by the algorithm occurred in the $m = 2373$ iteration, which involves the fact that the random number generated with the $\sigma = 0.5$mm standard deviation meant a search space that was too large while on the way to a global optimum [47].

The results of the local search algorithm and the adjusted local search algorithm trained on the SVR surrogate model are listed in Table 16. Considering the results the adjusted local search algorithm was several orders of magnitude more precise in the determination of the objective function even with a lower iteration number [47].

Table 16. Results of the optimization using local search algorithm [47]

	m	d_1 (mm)	d_2 (mm)	$E(\boldsymbol{d}_{opt})_{FEA}$ (kN²)
Local search	5000	109.184	35.372	0.051
Adjusted local search	3000	107.966	32.937	0.00025
Optimum shape		108	33	0

Owing to the opportunity of axisymmetric simplification, the running time of the finite element model only took 25 seconds on an Intel Core i5-8250U CPU. This computational need with 3000 iterations is below 21 hours [47].

4.5. Conclusions

The characteristics of the rubber bumpers of different shapes were determined with the help of the finite element method.

In the first optimization process, the SVR was used by means of open-source software to perform the optimization task.

The SVR method requires relatively few time-consuming learning points to treat non-linear multidimensional optimization problems. The teaching procedure producing

a small number of learning points and carried out by using the finite element method can be regarded as short. After the teaching procedure, the software provides a remarkably strong prediction for further multitude of parameters by dispensing with the time-consuming finite element calculations and relying on engineering intuition. For five design parameters, the shape optimization procedure proved to be fast and accurate. This regression process results in an approximation value of the objective function. The goodness of the calculation can be checked by finite element computation [47].

In the second optimization process, a two-dimensional shape optimization problem using a local stochastic search algorithm was introduced. As a metamodeling technique, SVR was selected for the training procedure. The SVR model required a lot less calculation than the finite element method, therefore this model was used to fine-tune the parameters of the local search algorithm. The algorithm with the adjusted parameters can be used directly in the shape optimization of rubber bumpers.

5. Summary of new scientific results

The following 4 items summarize the new research results:

Thesis 1
For closed-cell aluminium foams a novel geometrical reconstruction process based on μCT images was developed and the related finite element analysis of the structure in the elastic region was elaborated. It was proved that this geometrical reconstruction process including the finite element calculations is suitable for the detailed description of the real structures under compressive load.
This thesis is based on the following publication [T1].

Thesis 2
Closed-cell aluminium foam structure was approximated by a series of Weaire-Phelan unit cells and the developed CAD model was validated. Furthermore finite element model was established to determine the material response in a numerical way for compressive load which was validated by laboratory measurements. The developed process can be implemented in the design of closed-cell aluminium foam structures.
This thesis is based on the following publication [T2].

Thesis 3
Considering medical guidelines lattice structures from Ti6Al4V titanium alloy with the same porosity were designed and manufactured via direct metal laser sintering technology. Finite element models were then developed and validated by compression tests. It was proved that the

procedure can be implemented in the design process of patient-specific lattice structured hip implants.
This thesis is based on the following publications [T3, T4, T5].

Thesis 4
Support vector regression based optimization procedures were developed for the shape optimization of axisymmetric rubber bumpers. The introduced optimization processes with high accuracy can be implemented in the design practice relatively simply. The applicability of the novel methods was demonstrated on two- and five-dimensional shape optimization problems.
This thesis is based on the following publications [T6, T7].

6. References

6.1. Publications related to the theses

[T1] Mankovits, T., Varga, T.A., Manó, S., Kocsis, I.: *Compressive Response Determination of Closed-Cell Aluminium Foam and Linear-Elastic Finite Element Simulation of μCT-Based Directly Reconstructed Geometrical Models*, Strojniski Vestnik-Journal of Mechanical Engineering, 64:2, p. 105-113., 2018.

[T2] File, M., Cseke, R., Huri, D., Balogh, G., Mankovits, T.: *Finite element analysis of closed-cell aluminum foam approximated with Weaire-Phelan unit cell structure*, IOP Conference Series: Materials Science and Engineering, 1246, 012002, 2022.

[T3] Mankovits, T.: *Numerical analysis of unit cell models for orthopedic applications*, IOP Conference Series: Materials Science and Engineering, 393, 012019, 2018.

[T4] Alkentar, R., Huri, D., Mankovits, T.: *Numerical investigation of 3D lattice infill pattern cellular structure for orthopedic implant design*, Mechanisms and Machine Science, 109, p. 467-472., 2022.

[T5] Alkentar, R., File, M., Mankovits, T.: *Investigation of the Performance of Ti6Al4V Lattice Structures Designed for Biomedical Implants Using the Finite Element Method*, Materials, 15, 6335, 2022.

[T6] Mankovits, T., Szabó, T., Kocsis, I., Páczelt, I.: *Optimization of the Shape of Axi-Symmetric Rubber Bumpers*, Strojniski vestnik - Journal of Mechanical Engineering, 60:1, p. 61-71., 2014.

[T7] Huri, D., Mankovits, T.: *Parameter Selection of Local Search Algorithm for Design Optimization of Automotive Rubber Bumper*, Applied Sciences, 10:3584, 2020.

6.2. References used as supporting material

[1] Ashby, M.F., Evans, A.G., Fleck, N.A., Gibson, L.J.: *Metal Foams: A Design Guide*, Butterworth-Heinemann, Woburn, 2000.

[2] Mankovits, T., Varga, T.A., Manó, S., Kocsis, I.: *Compressive Response Determination of Closed-Cell Aluminium Foam and Linear-Elastic Finite Element Simulation of μCT-Based Directly Reconstructed Geometrical Models*, Strojniski Vestnik-Journal of Mechanical Engineering, 64:2, p. 105-113., 2018.

[3] Devivier, C., Tagliaferri, V., Trovalusci, F., Ucciardello, N.: *Mechanical characterization of open cell aluminium foams reinforced by nickel electro-deposition*, Materials and Design, 86, p. 272-278., 2015.

[4] Xiao, L., Song, W., Tang, H., Zhu, Z., Wang, J., Wang, H.: *High temperature compression properties of open-cell Ni– 20Cr foams produced by impregnation*, Materials and Design, 85, p. 47-53., 2015.

[5] Orbulov, I.N., Májlinger, K.: *Description of the compressive response of metal matrix syntactic foams*, Materials and Design, 49, p. 1-9., 2013.

[6] Peroni, L., Scapin, M., Fichera, C., Lehmhus, D., Weise, J., Baumeister, J., Avalle, M.: *Investigation of the mechanical behaviour of AISI 316L stainless steel syntactic foams at different strain-rates*, Composites Part B: Engineering, 66, p. 430-442., 2014.

[7] Pałka, K., Adamek, G., Jakubowicz, J.: *Compression behavior of Ti Foams with spherical and polyhedral pores*, Advanced Engineering Materials, vol. 18, no. 8, p. 1511-1518., 2016.

[8] Triawan, F., Kishimoto, K., Adachi, T., Inaba, K., Nakamura, T., Hashimura, T.: *The elastic behavior of aluminum alloy foam under uniaxial loading and bending conditions*, Acta Materialia, 60:6-7, p. 3084-3093., 2012.

[9] Hasan, A.: *An improved model for FE modeling and simulation of closed cell Al-alloy foams*, Advances in Materials Science and Engineering, ID 567390, 2010.

[10] Jang, W.Y., Kyriakides, S., Kraynik, A.M.: *On the compressive strength of open-cell metal foams with Kelvin and random cell structures*, International Journal of Solids and Structures, 47:21, p. 2872-2883., 2010.
[11] An, Y., Wen, C., Hodgson, P.D., Yang, C.: *Investigation of cell shape effect on the mechanical behaviour of open-cell metal foams*, Computational Materials Science, vol. 55, p. 1-9., 2012.
[12] Chen Y, Das R, Battley M, Xu Z.: *Compressive and shear strengths of the ductile closed-cell Kelvin and Weaire-Phelan foams along the lattice direction*, Thin-Walled Structures, 132, p. 237–249, 2018.
[13] Doroszko, M., Seweryn, A.: *Numerical modeling of the tensile deformation process of sintered 316L based on microtomography of porous mesostructures*, Materials and Design, 88, p. 493-504., 2015.
[14] Hangai, Y., Yamaguchi, R., Takahashi, S., Utsunomiya, T., Kuwazuru, O., Yoshikawa, N.: *Deformation behavior estimation of aluminum foam by X-ray CT image-based finite element analysis*, Metallurgical and Materials Transactions: A, 44:4, p. 1880-1887., 2013.
[15] Michailidis, N., Stergioudi, F., Omar, H., Papadoupoulos, D., Tsipas, D.N.: *Experimental and FEM analysis of the material response of porous metals imposed to mechanical loading*. Colloids and Surfaces A: Physicochemical and Engineering Aspects, 382:1-3., p. 124-131., 2010.
[16] File, M., Cseke, R., Huri, D., Balogh, G., Mankovits, T.: *Finite element analysis of closed-cell aluminum foam approximated with Weaire-Phelan unit cell structure*, IOP Conference Series: Materials Science and Engineering, 1246, 012002, 2022.
[17] Hamid, A., Gábora, A., Naeem, M.A., Kalácska, G., Mankovits, T.: *Effect of the manufacturing parameters on the pore size and porosity of closed-cell hybrid aluminum foams*, International Review of Applied Sciences And Engineering, 12:3, p. 230-237., 2021.
[18] Naeem, M.A., Gábora, A., Mankovits, T.: *Influence of the Manufacturing Parameters on the Compressive Properties of*

Closed Cell Aluminum Foams, Periodica Polytechnica-Mechanical Engineering, 64:2, p. 172-178., 2020.
[19] ISO 13314:2011 *Mechanical testing of metals — Ductility testing — Compression test for porous and cellular metals*, 2011.
[20] Agency for Healthcare Research and Quality: *Exhibit 19. HCUP Estimates of the Total Number of Target Procedures*, Rockville, MD, USA, 2012.
[21] Ulrich, S.D., Seyler, T.M., Bennett, D., Delanois, R.E., Saleh, K.J., Thongtrangan, I., Kuskowski, M., Cheng, E.Y., Sharkey, P.F., Parvizi, J., Stiehl, J.B., Mont, M.A..: Total Hip Arthroplasties: What Are the Reasons for Revision?, International Orthopaedics, 32, p. 597–604., 2008.
[22] Katz, J.L.: *Anisotropy of Young's Modulus of Bone*, Nature, 283, p. 106–107., 1980.
[23] Geetha, M., Singh, A.K., Asokamani, R., Gogia, A.K.: *Ti Based Biomaterials, the Ultimate Choice for Orthopaedic Implants - A Review*, Progress in Materials Science, 54:3, p. 397–425., 2009.
[24] Alkentar, R., Kladovasilakis, N., Tzetzis, D., Mankovits, T.: *Effects of Pore Size Parameters of Titanium Additively Manufactured Lattice Structures on the Osseointegration Process in Orthopedic Applications: A Comprehensive Review*, Crystals, 13:1, p. 1-16., 2023.
[25] Zadpoor, A.A.: *Mechanical performance of additively manufactured meta-biomaterials*, Acta Biomaterialia, 85, p. 41-59., 2019.
[26] Zhang, X.Z., Leary, M., Tang, H.P., Song, T., Qian, M.: *Selective electron beam manufactured Ti-6Al-4V lattice structures for orthopedic implant applications: Current status and outstanding challenges*, Current Opinion in Solid State and Materials Science, 22:3, p. 75-99., 2018.
[27] Alabort, E., Barba, D., Reed, R.C.: *Design of metallic bone by additive manufacturing*, Scripta Materialia, 164, p. 110-114., 2019.
[28] Zargarian, A., Esfahanian, M., Kadkhodapour, J., Ziaei-Rad, S., Zamani, D.: *On the fatigue behavior of additive manufactured*

lattice structures, Theoretical and Applied Fracture Mechanics, 100, p. 225-232., 2019.
[29] Bici, M., Brischetto , S., Campana, F., Ferro, C.G., Seclí, C., Varetti, S., Maggiore, P., Mazza, A.: *Development of a multifunctional panel for aerospace use through SLM additive manufacturing*. Procedia CIRP, 67, p. 215-220., 2018.
[30] Tan, J.H., Wong, W.L.E., Dalgarno, K.W.: *An overview of powder granulometry on feedstock and part performance in the selective laser melting process*, Additive Manufacturing, 18, p. 228-255., 2017.
[31] Khaing, M.W., Fuh, J.Y.H., Lu, L.: *Direct metal laser sintering for rapid tooling: Processing and characterisation of EOS parts*, Journal of Materials Processing Technology, 113, p. 269-272., 2001.
[32] EOS GmbH: *EOS Titanium Ti64 - Material Data Sheet*, 2017.
[33] EOS GmbH: *Technical data EOS M290*, 2022.
[34] Alkentar, R., File, M., Mankovits, T.: *Use of compression test to determine the Young's modulus of the titanium alloy Ti6Al4V manufactured via direct metal laser sintering*, International Review of Applied Sciences and Engineering, Online first, p. 1-7., 2023.
[35] Alkentar, R., File, M., Mankovits, T.: *Investigation of the Performance of Ti6Al4V Lattice Structures Designed for Biomedical Implants Using the Finite Element Method*, Materials, 15, 6335, 2022.
[36] Alkentar, R., Mankovits, T.: *A Study on the Shape and Dimensional Accuracy of Additively Manufactured Titanium Lattice Structures for Orthopedic Purposes*, Periodica Polytechnica Mechanical Engineering, 66:4, p. 336-343., 2022.
[37] Mankovits, T.: *Numerical analysis of unit cell models for orthopedic applications*, IOP Conference Series: Materials Science and Engineering, 393, 012019, 2018.
[38] Alkentar, R., Huri, D., Mankovits, T.: *Numerical investigation of 3D lattice infill pattern cellular structure for orthopedic implant design*, Mechanisms and Machine Science, 109, p. 467-472., 2022.

[39] Gáspár, P., Szászi, I., Bokor, J.: *Design of robust controllers for active vehicle suspension using the mixed synthesis*, Vehicle System Dynamics, 40:4, p. 193-228., 2003.
[40] Mankovits, T., Szabó, T., Kocsis, I., Páczelt, I.: *Optimization of the Shape of Axi-Symmetric Rubber Bumpers*, Strojniski vestnik - Journal of Mechanical Engineering, 60:1, p. 61-71., 2014.
[41] Kim, J.J., Kim, H.Y.: *Shape design of an engine mount by a method of parameter optimization*, Computers and Structures, 65:5, p. 725-731., 1997.
[42] Choi, K.K., Duan, W.: *Design sensitivity analysis and shape optimization of structural components with hyperelastic material* Computer Methods in Applied Mechanics and Engineering, 187, p. 219-243., 2000.
[43] Ramachandran, T., Padmanaban, K.P., Nesamani, P.: *Modeling and analysis of IC engine mount using finite element method and RSM*, Procedia Engineering, 38, p. 1683-1692., 2012.
[44] Lee, J.S., Kim, S.C.: *Optimal design of engine mount rubber considering stiffness and fatigue strength*, Journal of Automobile Engineering, 221:7, p. 823-835., 2007.
[45] Bonet, J., Wood, R.D.: *Nonlinear continuum mechanics for finite element analysis*, Cambridge University Press, Cambridge, p. 248., 1997.
[46] Norvig, P.; Russell, S.J.: *Mesterséges Intelligencia Modern Megközelítésben*, Panem Kiadó Kft., Budapest, 2005.
[47] Huri, D., Mankovits, T.: *Parameter Selection of Local Search Algorithm for Design Optimization of Automotive Rubber Bumper*, Applied Sciences, 10:3584, 2020.
[48] ISO 7743:2017 *Rubber, vulcanized or thermoplastic - Determination of compression stress-strain properties*, 2017.
[49] Huri, D., Mankovits, T.: *Comparison of the material models in rubber finite element analysis*, IOP Conference Series: Materials Science and Engineering, 393:012018, 2018.
[50] Huri, D.: *Incompressibility and mesh sensitivity analysis in finite element simulation of rubbers*, International Review of Applied Sciences and Engineering, 7:1, p. 7-12, 2016.

[51] Bathe K.J.: *Finite Element Procedures*, Prentice Hall, New Jersey, 1996.
[52] Mankovits T., Szabó T.: *Finite element analysis of rubber bumper used in air-spring*, Procedia Engineering, 48, p. 388-395., 2012.
[53] Drucker, H., Bruges, C.J.C., Kaufman, L., Smola, A.J., Vapnik, V.: *Support vector regression machines*, Advances in Neural Information Processing System, 9, p. 10700-10708., 1997.
[54] Haykin, S.: *Neural networks and learning machines*, Pearson Prentice Hall, Upper Saddle River, 2009.
[55] Cruz Gómez, M.A., Gallardo-Hernandéz, E.A., Vite Torres, M., Pena Bautista, A.: *A rubber steel friction in contaminated contacts*, Wear, 302, p. 1421-1425., 2013.
[56] Huri, D., Mankovits, T.: *Automotive rubber part design using machine learning*, IOP Conference Series: Materials Science and Engineering, 659:012022, 2019.